

Full length article

Noise-robust ptychography using dynamic sigmoid-remolding

Chuangchuang Chen^a, Honggang Gu^{a,b,c,*}, Shiyuan Liu^{a,b,*}^a State Key Laboratory of Intelligent Manufacturing Equipment and Technology, Huazhong University of Science and Technology, Wuhan, Hubei 430074, China^b Optics Valley Laboratory, Wuhan, Hubei 430074, China^c Guangdong HUST Industrial Technology Research Institute, Guangdong Provincial Key Laboratory of Manufacturing Equipment Digitization, Dongguan, Guangdong 523003, China

ARTICLE INFO

Keywords:

Ptychography
Noise robust
Dynamic update
Computational imaging

ABSTRACT

Ptychography is a promising technique for phase retrieval, allowing for super-resolution imaging with a coherent beam source that shifts. The complex transmission function of illumination and object can be retrieved with the support of a ptychographic iterative kernel. When subjected to noisy datasets, conventional reconstruction algorithms can easily be trapped in local minima or even fail to convergence. The present work proposes a new approach called dynamic sigmoid-remolding ptychographic iterative engine (dsPIE) that relies on a dynamic convex optimization strategy. The dsPIE method is designed to improve the robustness in ptychography against detector noise. Computational and experimental results show that the proposed dsPIE method exhibits high robustness and finer reconstructed stability for mixed detector noises that conventional PIE algorithms typically struggle to converge. This method has important implications for the field of computational imaging in high-noise environments.

1. Introduction

Ptychography is a scanning coherent diffractive imaging (CDI) technique [1] that relies on an approach of improved phase retrieval method by shifting illumination with no need for imaging lenses [2]. It solves images beyond the diffraction limit and achieves optical super-resolution which is only determined by the wavelength of the radiation source and the effective numerical aperture of the diffraction intensity detector [3]. In recent years, with the improvement of coherent light sources [4,5], ptychography has been widely applied as a super-resolution imaging method in biomedical imaging [6–8], three-dimensional (3D) nanostructure characterization [9], and integrated circuit (IC) manufacture [10], etc.

In practical applications, the instabilities of system, such as incoherence of illumination, probe drifting, detector noise, nonuniformity of specimen, etc., will significantly decrease the performance of ptychography. Researchers have conducted further studies around these issues for several years, and some remarkable results have been reported. For example, to deal with the incoherence of illumination, Thibault *et al.* proposed a mixed-state formulation to match the state of partial coherence by means of decomposing the mixed state into a set of fully

coherent illumination modes in ptychography [11]. In Huijts *et al.*'s research, the incoherence of broadband illumination was reduced to fully coherent diffraction by a monochromatized formula in the ptychographic process [12]. Groups of position correction scenarios based on cross-correlation were presented to eliminate the influences of the probe drifting [13–15], axial calibration [16,17], and scattering effects [18,19] on ptychography. Additionally, Tang *et al.* introduced a variable-aperture to eliminate the requirement for mechanical aperture scanning [20], Li *et al.* proposed a co-phase error detection approach in ptychography, enabling the simultaneous detection of piston, tip, tilt, and decenter errors [21]. The presence of noise introduces additional complexity to ptychography, rendering it a more challenging and non-convex optimization problem. To reduce the detector noise, one strategy is direct noise removal, which is however usually restricted by specific cases [22]. Another strategy is to improve the robustness of the algorithm, such as the least-squares solver for generalized maximum-likelihood ptychography [23], adaptive iterative guided filtering for suppressing background noise [24], and momentum-accelerated ptychographic iterative engine (mPIE) methods [25], which are capable to improve the convergence speed by enhancing the robustness to noises. Besides, Wu *et al.* [26] utilized a loss correction algorithm with adaptive

* Corresponding authors at: State Key Laboratory of Intelligent Manufacturing Equipment and Technology, Huazhong University of Science and Technology, Wuhan, Hubei 430074, China.

E-mail addresses: hongganggu@hust.edu.cn (H. Gu), shyliu@hust.edu.cn (S. Liu).

<https://doi.org/10.1016/j.optlastec.2023.110510>

Received 19 July 2023; Received in revised form 24 October 2023; Accepted 22 December 2023

0030-3992/© 2023 Elsevier Ltd. All rights reserved.

step size, effectively mitigating noise during the convergence process. Zuo et al. [27] also proposed an adaptive step-size strategy in Fourier ptychography, and proved that the optimization of step size in ptychography contributes to the enhancement in reconstruction.

In this paper, we focus on the convergence behavior of ptychography under detector noise conditions, and demonstrate a general regularized optimization with a dynamic sigmoid decision function that we call dynamic sigmoid-remolding PIE (dsPIE), to improve the robustness of ptychography with mixed noisy datasets. In section 2, we firstly formulate the measured diffraction modulus projection constraint under noisy conditions in measurement as an unconstrained convex minimization problem. And then, by analyzing the convergence behaviors of the weight functions in ptychography, the dsPIE method is introduced to improve the reconstructed quality and robustness against noise. Section 3 and Section 4 presents the simulations and experimental results, respectively. Results demonstrate that the proposed dsPIE presents an ability of high robustness towards noise with finer convergence than existing PIE algorithms. Finally, the discussion and conclusion are summarized in Section 5.

2. Theory and methods

2.1. Weight functions in ptychography

Ptychography can be considered as a constrained optimization problem, whose solution is defined by a common complex-valued coherent illumination function $P(r)$ and a complex-valued transmission function $O(r)$, and the two-dimensional (2D) exit wave ψ_{jr} is given by

$$\psi_{jr} = O_{jr} \cdot P_{jr}; \forall r \in R, \quad (1)$$

where P_{jr} is a 2D coherent illumination function called the probe, O_{jr} is the local region r of the object transmission function located at the j -th (where $j = 1, 2, \dots, J$) probe position, and R represents a set comprising all scanning positions j . A given propagator \mathcal{F} is applied to propagate the exit wave radiation ψ_{jr} in the real space to the reciprocal space generating the specific complex-valued diffracted wavefront Ψ_{ju} , as expressed as

$$\Psi_{ju} = \mathcal{F}[\psi_{jr}], \quad (2)$$

herein, the propagator \mathcal{F} denotes the fast Fourier transform (FFT) as a particular operator among various phase retrieval methods, such as the conventional CDI [28,29], Bragg ptychography [30], Fourier ptychography [27,31], etc. Since Fraunhofer propagation and its inverse formula act as an analog computer to perform Fourier transformation, the FFT can be applied to accelerate the ptychographic solving speed.

Eqs. (1) and (2) assume an ideal scenario where the light-matter interaction in Fraunhofer diffraction follows the transmission geometry that is noise-free. However, considering the detector noise during the diffraction data acquisition process, higher diffraction orders exhibit a decrease in intensity with respect to the angle of diffraction, resulting in lower signal-to-noise (SNR) for higher-order diffraction images compared to lower-order ones in measurement with noise, thus, the captured diffraction pattern I_{ju} in the far-field is mixed with detector noise, we utilized a widely-used noise model in photography to analyze the primary noise sources in the acquisition of diffracted images [32,33], the properties of diffraction pattern mixed with detector noise can be modeled as

$$I_{ju} \sim \text{Poisson}(t \cdot \alpha \cdot |\Psi_{ju}|^2) \cdot g + \text{Poisson}(t \cdot g \cdot D) + \text{Normal}(0, \sqrt{\sigma_{\text{read}}^2 \cdot g^2 + \sigma_{\text{ADC}}^2}) \quad (3)$$

where t , α , and g stands for the exposure time, the quantum efficiency, and the analog amplifier in detector, and D is the dark current noise. The σ_{read} and σ_{ADC} denote the variances of readout process and analog-to-digital converter (ADC) process in detector, respectively.

When a scene radiant flux Ψ_{ju} reaches the detector with a given exposure time t , the accumulated photons are converted to electrons in proportion to their number with a given QE α , which introduces photon noise. Additionally, some electrons are randomly released simultaneously, leading to dark noise D . The total number of electrons follows a Poisson distribution. Additionally, both readout noise and ADC noise are additive noise sources that are independent of the scene and exposure, and typically follows a zero-mean Gaussian distribution. Thus, the measured diffraction I_{ju} is coupled with the mixed noises as

$$I_{ju} = N_{\Psi} + N_D + N_{\text{add}} \quad (4)$$

where N_{Ψ} denotes the diffraction intensity mixed with photon noise, N_D denotes the Poisson distributed dark noise, and N_{add} is the Gaussian distributed additive noise.

The ptychographic reconstruction algorithm typically starts with an initial guess of the object $O(r)$ and sometimes the probe $P(r)$ if the probe is not given in advance, then it proceeds with exit wave function ψ_{jr} and gets the diffracted wavefront Ψ_{ju} . A new exit wave ψ'_{jr} is generated by the inverse FFT propagator of Ψ_{ju} replacing the amplitude information with the square root of I_{ju}

$$\psi'_{jr} = \mathcal{F}^{-1} \left[\sqrt{I_{ju}} \frac{\Psi_{ju}}{|\Psi_{ju}|} \right] = \mathcal{F}^{-1} \left[\sqrt{N_{\Psi} + N_D + N_{\text{add}}} \frac{\Psi_{ju}}{|\Psi_{ju}|} \right] \quad (5)$$

The update strategy described in Eq. (2) and Eq. (5) follows the principles of alternating projections. In an ideal scenario without noise, ψ_{jr} would provide an improved estimation of ψ_{jr} by enforcing the modulus constraint on the diffraction intensity. However, the presence of detector noise makes the updated ψ'_{jr} to be coupled with ambiguity. Ptychography solves the complex object $O(r)$ and the probe $P(r)$ simultaneously by minimizing the L2-norm based cost function as

$$\hat{O}(r), \hat{P}(r) = \arg \min_{O(r), P(r)} \sum_j (\sqrt{I_{ju}} - |\Psi_{ju}|)^2 \quad (6)$$

In practice, the presence of detector perturbation noise poses a significant challenge as Eq. (6) becomes a non-convex optimization problem, frequently leading to ptychographic reconstructions being trapped in local minima. Although further improvements in ptychographic iterative engine (PIE) have shown promise in phase retrieval, its effectiveness is limited when dealing with high levels of noise.

The PIE algorithms are usually sequentially operated in a specific update order, such algorithms as PIE[2], ePIE [28], and rPIE [25]. Here we give a general update expression in the ptychographic update progress

$$O'_{jr} = O_{jr} + w_{jr} \frac{\text{conj}(P_{jr})}{|P_{jr}|^2 + \varepsilon} (\psi'_{jr} - \psi_{jr}) \quad (7)$$

where w_{jr} is the weight function of the updated object estimate, and ε is a small real number to avoid zero-divide infinity. Here, a comparison of weight functions for the PIE, ePIE, and rPIE are given by

$$w_{jr} = \begin{cases} |P_{jr}|^3 / [|P_{jr}|_{\max} (|P_{jr}|^2 + \alpha |P_{jr}|_{\max}^2)]; & w_{jr} \in \text{PIE} \\ \alpha |P_{jr}|^2 / |P_{jr}|_{\max}^2; & w_{jr} \in \text{ePIE} \\ |P_{jr}|^2 / [\alpha |P_{jr}|_{\max}^2 + (1 - \alpha) |P_{jr}|^2]; & w_{jr} \in \text{rPIE} \end{cases} \quad (8)$$

where α denotes the step size of the weight function w_{jr} .

It turns out that ePIE makes a very basic change from PIE by replacing the normalized probe magnitude information with the normalized probe intensity, while rPIE can be interpreted as a regularized version of ePIE. To straightforwardly demonstrate the influences of these different weight functions, Fig. 1 illustrates the distribution curves of the beam wavefront for different weight functions with different step sizes of α . The beam shape of the probe $P(r)$ is assumed as a complex-

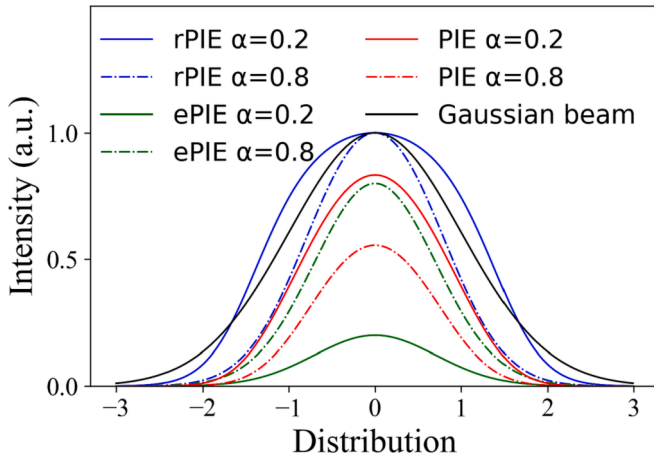


Fig. 1. Distribution curves of the beam wavefront of the indicative object weight functions of typical PIE algorithms. The black curve shows a gaussian beam wavefront distribution as a reference. Blue, green, and red curves represent the weight functions of the rPIE, ePIE, and PIE, respectively. (For interpretation of the references to colour in this figure legend, the reader is referred to the web version of this article.)

valued Gaussian distribution, which is the case for the most common situations of incidence beam. The bandwidth of each weighting distribution varies significantly among different types of weight functions. rPIE exhibits a broader bandwidth (blue curves), indicating improved performance in regions where the probe modulus is dim [34], resulting in faster minimization. Furthermore, the weight functions are highly sensitive to the step size parameter α . This sensitivity adds complexity to the selection of an optimal step size for practical ptychography applications. Careful consideration and experimentation are necessary to choose a suitable step size that ensures accurate and reliable results.

It is important to note that the PIE family algorithms, which employ a “minibatch stochastic gradient descent” approach with the partial Lipschitz constant as the step size [35], exhibit similar performance under ideal (noise-free) conditions when an appropriate step size is chosen. However, in practical scenarios involving problematic noisy datasets described in Eq. (3), the convergence performance of these algorithms may be significantly and differently affected. This degradation in performance can be attributed to the non-convex nature of the phase retrieval problem and the improper choice of step size [36]. PIE-type algorithms, being incremental gradient approaches, are particularly sensitive to noise and often struggle to converge to satisfactory solutions when a constant step size is used [27]. Theoretical analysis above and experimental results in the subsequent section further support this observation.

2.2. Dynamic sigmoid-remolding ptychography (dsPIE)

Ideally, the rigorous alternating projection approach and its inverse form align perfectly with the ptychographic update, satisfying both the modulus constraints in the detector plane and the “overlapping” constraints in the sample plane. This alignment allows for a successful reconstruction. However, in the presence of mixed noise, the quality of reconstruction can be compromised as the modulus constraints are disrupted by the mixture of noises. Fundamentally, the phase retrieval problem in this issue represents a non-convex and non-linear optimization problem. Few phase retrieval strategies guarantee to “skip over” all local minima and achieve theoretical global convergence, even in noise-free conditions.

To address the aforementioned issues related to noise, we introduce a new dynamic convex optimization approach known as dsPIE, which is inspired from the concept of relaxation in convex optimization theory [37]. The dsPIE algorithm aims to dynamically adapt and optimize the

reconstruction process by iteratively updating and refining the estimates of $O(r)$ and $P(r)$ alternately. The schematic view of the dsPIE is depicted in Fig. 2 concisely. Our objective is to minimize the projection distance between the object A and the probe B along line P. The following steps outline the process:

Step 0: The dsPIE algorithm starts by initializing the probe and object with an initial guess, which can be randomly generated or based on *prior* knowledge, following a common practice in convex optimization algorithms.

Step 1: The dsPIE algorithm iteratively applies gradient descent methods such as the PIE family, difference map (DM) [38], or the Relaxed Averaged Alternating Reflection (RAAR) algorithm [39]. This process leads to the acquisition of a local optimum solution. However, in cases where the data is affected by mixed noise, the algorithm may become trapped in a local minimum, failing to reach the global optimum. Nevertheless, the obtained solution still retains certain characteristics of the ideal probe or object.

Step 2: Recognizing that incorporating partial knowledge of the probe or specimen greatly enhances reconstruction robustness and precision in ptychography [4,40], we utilize the retrieved probe data as *prior* knowledge with a tiny step size. Simultaneously, a random perturbation is applied on the retrieved object as a new initialization with a relatively large step size. This approach allows the iterations to escape the previously trapped local minimum in Step 1, resulting in an object estimate closer to the ideal.

Step 3: Similarly, we modify the ptychographic workflow from Step 2 by interchanging the roles of the retrieved probe and object. The retrieved object from Step 2 is now used as *prior* knowledge, and the retrieved probe undergoes relaxation with the introduction of a random perturbation. As a result, the iterations in this step yield a more refined solution for the retrieved probe compared to the previous step.

By repeating steps 2 and 3, the dsPIE algorithm progressively refines the estimates of the object and probe. To achieve this, we introduce a revised sigmoid function $S(n, flag)$ to modulate the step size dynamically in ptychography. Additionally, we incorporate a random remolding matrix as a perturbation to the objective function, as given in Eq. (9), facilitating relaxation from the local minimum. These modifications enhance the convergence and effectiveness of the dsPIE algorithm in achieving improved reconstructions of the object and probe globally. The update function of dsPIE is optimized as

$$O'_{jr} = \begin{cases} \text{Random}(O_{jr}); & \forall n = N \\ O_{jr} + S(n, flag) w_{jr} \frac{\text{conj}(P_{jr})}{|P_{jr}|^2 + \epsilon} (P'_{jr} - P_{jr}); & \text{otherwise} \end{cases} \quad (9)$$

Where $\text{Random}(O_{jr})$ gives a uniform distributed random with the same matrix shape as O_{jr} (complex valued matrix), performed as a powerful remolding impulse to the update function in Eq. (9). $S(n, flag)$ is a sigmoid function to modulate the step size of the update function in dsPIE, given by

$$S(n, flag) = \begin{cases} 1 - \frac{1}{1 + e^{(N-n)}}; & flag = 1 \\ \frac{1}{1 + e^{(N-n)}}; & flag = 0 \end{cases} \quad (10)$$

where N is the dynamic sigmoid impulse moment in the evolution of dsPIE, N_{probe} and N_{obj} are two typical formulas of the sigmoid impulse moment for the probe and object, respectively. $flag$ is a binary switch that changes with the update of N_{probe} or N_{obj} . The function $S(n, flag)$ significantly decreases with the iteration number n in case of $flag = 0$ and increasing while $flag = 1$. This behavior of $S(n, flag)$ plays a crucial role in the dsPIE algorithm, as it modulates the weight functions during the iterations to ensure effective convergence and refinement of the reconstruction process.

As previously mentioned, the presence of mixed noisy datasets makes it challenging to accurately evaluate the convergence of ptychography

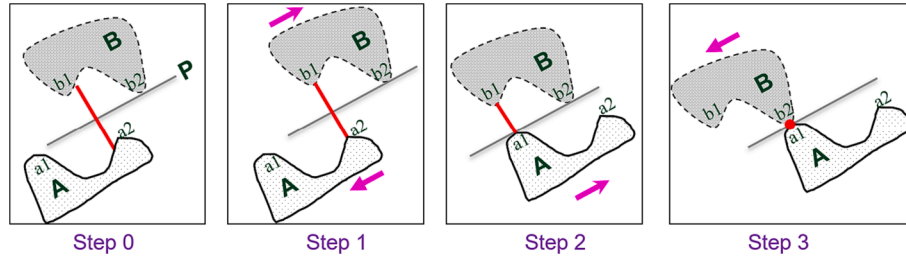


Fig. 2. Schematic view of how the dsPIE skips over the local minima. A and B are two groups of non-convex datasets which represent the probe and the object. a1, a2, b1, b2 represent key inflection points in A and B, respectively. The line P indicates the alternating projections.

using the mean square error (MSE) of diffracted intensities. In many instances, despite the MSE of diffracted intensities reaching its minimum after multiple iterations, the reconstructed object or probe may still remain trapped in a local minimum. To address this issue, we propose a solution that involves using the structural similarity index measure (SSIM) [41] of the updated exit wave ψ_{jr} in real space. The SSIM serves as an incremental criterion for determining the dynamic sigmoid impulse moments of N_{probe} and N_{obj} .

$$\text{ssim}_n = \frac{1}{J} \sum_j \text{SSIM}(\psi_{jr-n}, \psi_{jr-n-1}) \quad (11)$$

where J is the number of the scanning positions in ptychography, n refers to the iteration moments. When the convergence in ptychography is trapped in local minimum during evolution, the structure of the incremental exit waves exhibits a high degree of similarity. This similarity is reflected in the value of ssim_n , which approaches 1. As the result, Eq. (11) serves as an improved decision function for determining the dynamic sigmoid impulse moments of N_{probe} and N_{obj} .

Let's summarize the mathematical view of the dsPIE workflow. As the iterations progress, the object and probe gradually converge, and the ssim_n value increases. When ssim_n approaches 1 at the n -th iteration, N_{probe} is assigned the value n , triggering the flag for the object.

Algorithm: dsPIE

Initialize: flag = 1, t = 0, T=3 (Remolding steps)

n -th Loop

for j=1:J (different incident positions)

- Exit wave update

$$\psi_{jr} = P_{jr} \cdot O_{jr}; \psi'_{ju} = \mathcal{F}[\psi_{jr}]; \psi'_{ju} = \sqrt{I_{ju}} \frac{\psi_{ju}}{|\psi_{ju}|}; \psi'_{jr} = \mathcal{F}^{-1}[\psi'_{ju}]$$

- Exit wave incremental deviation definition

$$\text{ssim}_n = \frac{1}{J} \sum_j \text{SSIM}(\psi_{jr-n}, \psi_{jr-n-1})$$

if $\text{ssim}_n > 0.95$ and $t < T$:

- dsPIE remolding

$N=n$

if flag:

$$R(O'_{jr}) = \text{Random}(O'_{jr})$$

$$S_{\text{obj}}(n, \text{flag}) = 1 - \frac{1}{1 + e^{(N-n)}}$$

$$S_{\text{probe}}(n, \text{flag}) = \frac{1}{1 + e^{(N-n)}}$$

else:

$$R(P'_{jr}) = \text{Random}(P'_{jr})$$

$$S_{\text{obj}}(n, \text{flag}) = \frac{1}{1 + e^{(N-n)}}$$

$$S_{\text{probe}}(n, \text{flag}) = 1 - \frac{1}{1 + e^{(N-n)}}$$

flag = not (flag), t=t+1

else:

- dsPIE update

$$O'_{jr} = O_{jr} + S(n, \text{flag}) w(jr) \frac{\text{conj}(P_{jr})}{|P_{jr}|_{\text{max}}} \Delta \psi_{jr}$$

$$P'_{jr} = P_{jr} + S(n, \text{flag}) w(jr) \frac{\text{conj}(O_{jr})}{|O_{jr}|_{\text{max}}} \Delta \psi_{jr}$$

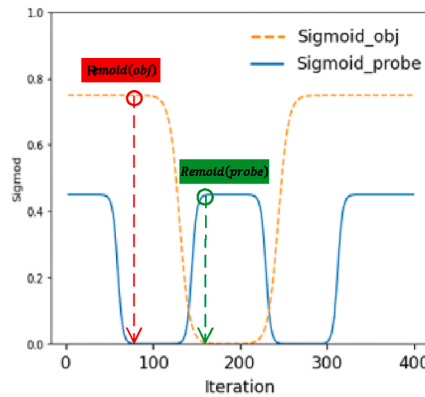


Fig. 3. Schematic pseudocode flow of the dsPIE. Red dashed arrow lines indicate the sigmoid points of the object N_{obj} and green solid arrow lines indicate the sigmoid points of the probe N_{probe} in the iteration process of dsPIE. (For interpretation of the references to colour in this figure legend, the reader is referred to the web version of this article.)

Simultaneously, a remolding matrix described in Eq. (9) is applied to the object O'_{jr} , facilitating its convergence to escape from the local minimum. The same process applies to N_{obj} . Since the probe function $P(r)$ maps complete scanning views of the object in ptychography, the probe often converges faster than the object. Therefore, a remolding matrix is initially applied to $O(r)$ in the first remolding step, followed by alternating updates of N_{probe} and N_{obj} . In practical use, the dynamic sigmoid impulse moments of N_{probe} and N_{obj} can also be manually chosen based on experimental experience, allowing for more flexibility and control in the optimization process of the dsPIE algorithm. Typically, a globally refined reconstruction can be achieved within a few remolding steps, typically no more than 3 steps in our experimental validation. Fig. 3 provides a schematic pseudocode flow of the dsPIE algorithm.

3. Numerical simulations

In this section, we numerically compare the performance of three algorithms: ePIE, mPIE, and dsPIE, to assess the effectiveness of the proposed dsPIE method in presence of varying levels of noises. Since the step size of the PIE algorithms greatly influence their convergence performance, we selected optimal step sizes ($\alpha = 0.15$, $\beta = 0.8$) for ePIE to meet with the best convergence and stability. For mPIE, we followed the suggested settings from Andrew's published work [25] to simplify the tuning process. There are several important implementation considerations for reconstruction using these PIE algorithms. Firstly, all of these incremental PIE algorithms utilize the same initial random guess for both the probe and the object. Secondly, all these PIE algorithms share a common architecture, with the update function being the only variation. Additionally, we repeated 5 trials of each algorithm in every single simulation in case of evading the disturbance of single random initialization in ptychography.

We use a 2D complex-valued object that combines the amplitude information of the "USAF target" and the phase information of the "cameraman" image for the simulations. It is important to note that the complex-valued object has been [0,1] scaled in phase, resulting in a relatively weak power distribution in the phase component. Additionally, a programmed gaussian beam with a constant plane wave in phase is designed as the incident probe, as shown in Fig. 4(b). The size of probe is set to be 125 pixels in diameter. To capture the diffraction patterns, we employ a 16-bit camera with 256x256 pixels. The probe is scanned over a 9x9 grid with a step size of 20 pixels, and we introduce a 10 % random offset during the scanning process to prevent periodic artifacts from

occurring in ptychography [42]. In total, 81 frames of diffraction patterns are recorded. To simulate real-world scenarios, we scale the diffraction patterns to the range [0, 2¹⁶-1], mimicking the dynamic range of a 16-bit camera. Values below 1 are discarded as they typically represent background noise. To account for the noise of detector measurements under realistic mixed noise conditions in ptychography [43,44], we add different distributions of noise, including Gaussian, Poisson, and a mixture of Poisson and Gaussian noise, to the diffraction patterns. The noise levels are measured using the SNR and vary from 45 dB to 15 dB, as shown in Fig. 4(a).

The simulation results quantify the reconstruction performances for the ptychography algorithms. Three groups of reconstructions proceeded with 300 iterations under varying levels of noises, resulting in a series of retrieved results of ePIE, mPIE, and dsPIE, respectively, as shown in Fig. 5. Seeing that the conventional ePIE is highly sensitive to noise, especially the Gaussian-distributed noise (Fig. 5(a)). When the SNR of noise decreases to 15 dB, the reconstructed object shows an intense reduction in both resolution and fidelity in terms of amplitude. Moreover, due to the low entropy of the probe in phase, as shown in Fig. 4(b), the phases of the reconstructed object exhibit significant oscillations that is trapped into local minimum and fail to converge under noise. Introducing a more complex structure to the probe can potentially address this issue by increasing the information entropy of the probe [45]. Nevertheless, the reconstructed probes demonstrate a high level of consistency with the ground truth in both amplitude and phase, regardless of the level of noise. The reconstructions obtained with mPIE show similar performance to ePIE in terms of amplitude in cases of low levels of noise. However, mPIE demonstrates improved reconstructions in terms of phase, as shown in Fig. 5(b). When faced with a heavy level of noise, particularly at a SNR of 15 dB, the reconstructed object exhibits improved resolution in amplitude but still lacks fidelity, especially in the presence of Gaussian noise and mixed noise. This can be attributed to the incorporation of momentum and regularization techniques in the mPIE algorithm. Furthermore, the reconstructed probe of mPIE exhibits prominent fluctuations in phase, and these fluctuations are also reflected in the corresponding reconstructed object. These fluctuations are introduced by the overshoot of momentum-acceleration in mPIE, particularly when the probe has a relatively simple structure with low information entropy.

Compared to ePIE and mPIE, the proposed dsPIE reveals the best stable and robust performance in reconstructions of both the object and the probe across varying levels of noises, as demonstrated in Fig. 5(c).

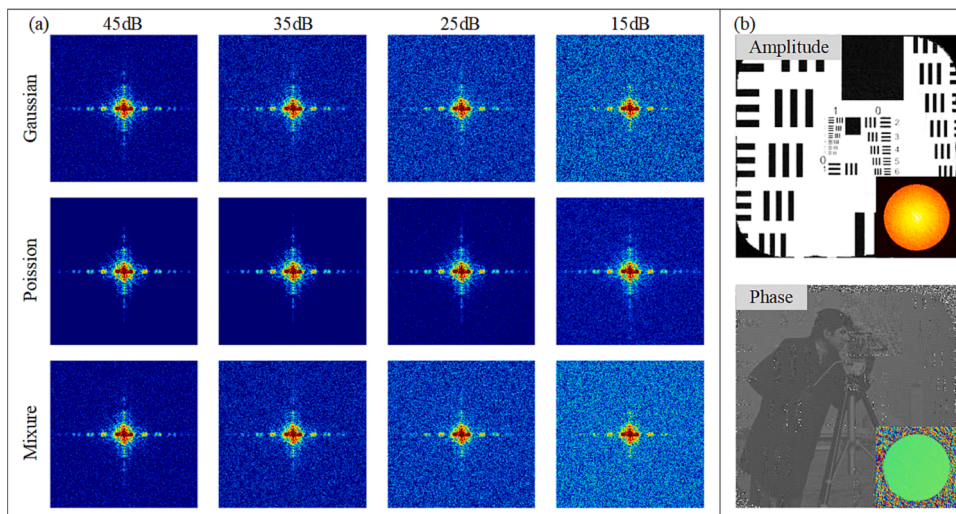


Fig. 4. (a) Representative diffraction patterns with different distributions of noises (Gaussian, Poisson, and a mixture of Gaussian and Poisson noise in rows) and varying levels of noise (ranging from 45 dB to 15 dB in columns), log scaled. (b) The reconstructed complex-valued object and the corresponding probe of dsPIE with noise free diffractions.

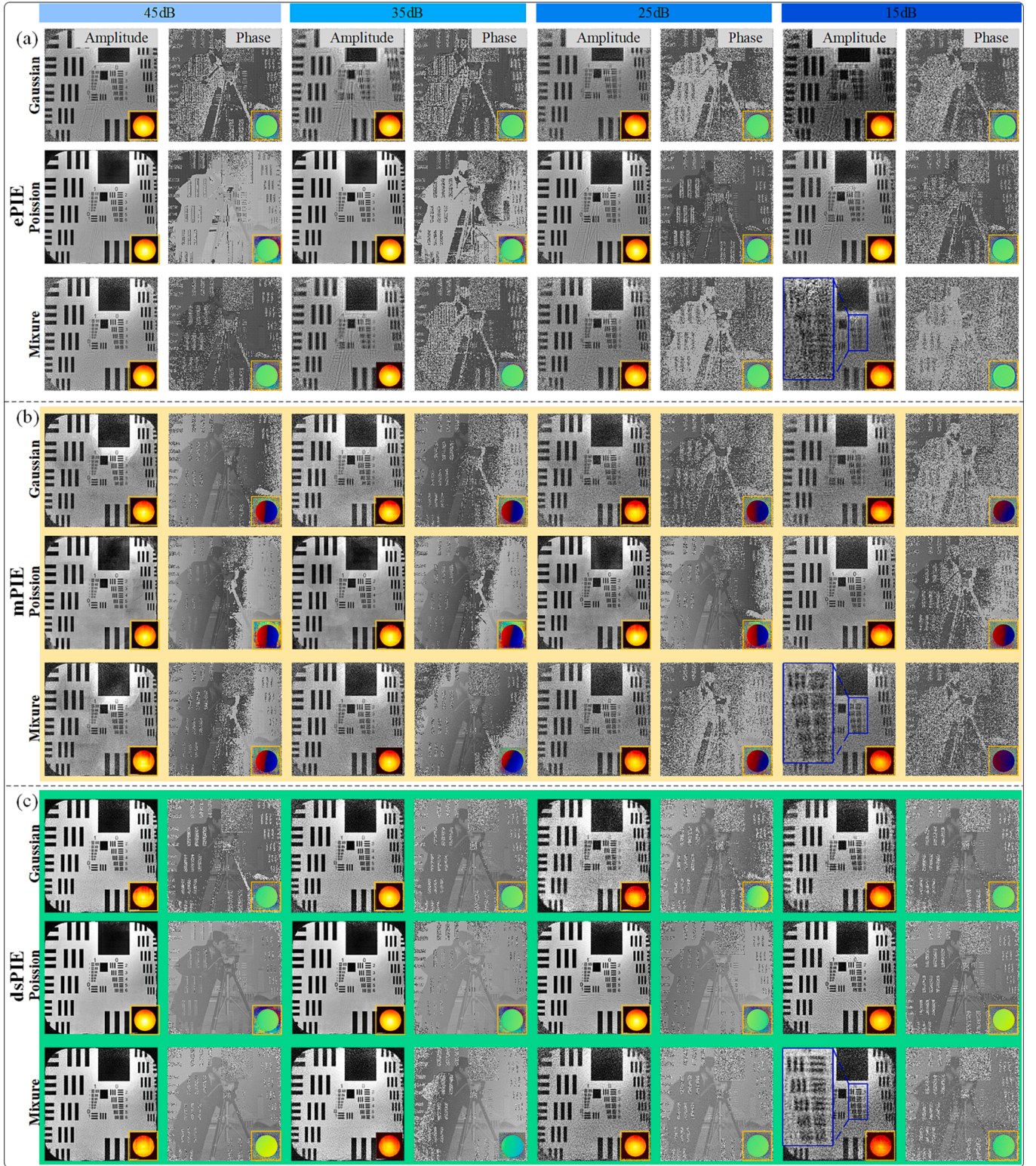


Fig. 5. Reconstructions of different levels of noises. (a)-(c) show the results for the rPIE, mPIE, and dsPIE with different noise distributions (Gaussian, Poisson, and a mixture of Gaussian and Poisson noise in columns) and varying levels of noises (ranging from 45 dB to 15 dB in rows), respectively. The corresponding reconstructed probes are displayed in the yellow insert within the subfigures. (For interpretation of the references to colour in this figure legend, the reader is referred to the web version of this article.)

Seeing that the dsPIE achieves highly resolved reconstructions across Gaussian, Poisson, and mixed Gaussian-Poisson noise, especially when the SNR of the noise is above 35 dB. Specifically, the line pairs of Group (1) are clearly distinguished in the amplitude reconstructions obtained

with dsPIE. Besides, the reconstructed images in phase also exhibit the highest consistency with the ground truth across varying levels of noise. As the level of noise increases, the benefits of dsPIE become more evident. Specifically when the SNR of the noise is below 25 dB, the

reconstructed objects still appear to have the highest level of clarity and fidelity in both the magnitude and phase. Furthermore, the reconstructed probe shows excellent uniformity and high consistency with the ideal wavefront. This highlights the superior performance of the proposed dsPIE algorithm in handling challenging noise conditions, and achieving highly robust convergence against detector noise.

Furthermore, it's worth noting that there is an inconsistency in the phase reconstructions. This inconsistency arises from the fact that the amplitude image is a binary USAF resolution target. In ptychography, accurately reconstructing the phase information in the zero-value regions of the binary amplitude image can be challenging. The phase values in these regions are less constrained and can vary randomly between 0 and 2π during the reconstruction process. Besides, the specimen's weak power distribution in phase (phase information scaled from 0 to 1 in our simulations) further compounds the challenge of achieving a globally optimized reconstruction in phase.

Fig. 6 zooms the results of ePIE, mPIE, and dsPIE under a heavy mixture noise with a SNR of 15 dB. Despite the challenging conditions of mixed noise, dsPIE demonstrates excellent reconstructions for both the object and the probe. Specifically, in the amplitude image, the line pairs of Group 0 reconstructed using dsPIE exhibit clear resolution and high contrast, while the results obtained from ePIE and mPIE reconstructions are severely contaminated by noise. Moreover, the phase image reconstructed by dsPIE demonstrates high fidelity compared to ePIE and mPIE, indicating the robustness and accuracy of dsPIE in handling challenging noise scenarios. These results highlight the remarkable stability and reliability of the dsPIE algorithm, making it a valuable tool for noise-robust ptychographic reconstructions.

To further quantitatively evaluate the convergence performance of dsPIE, we computed the SSIM between the reconstructed image in amplitude and the ground truth under different noise conditions. The results are shown in Fig. 7. It is evident that dsPIE consistently achieves the highest SSIM values across the range of noise levels, outperforming both ePIE and mPIE. Fig. 7 highlights two notable phenomena in the context of ptychography towards noise. Firstly, it is observed that ptychographic algorithms exhibit better robustness against Poisson noise compared to Gaussian noise, indicating that optimizing detector noise, particularly focusing on reducing the impact of Gaussian noise, can significantly enhance the performance of ptychography. Secondly, the trend of SSIM for the reconstructed amplitude is linearly consistent with the change in noise energy.

To better explain the convergence behavior of dsPIE under heavy noise conditions, we monitored the evolution of the SSIM between the

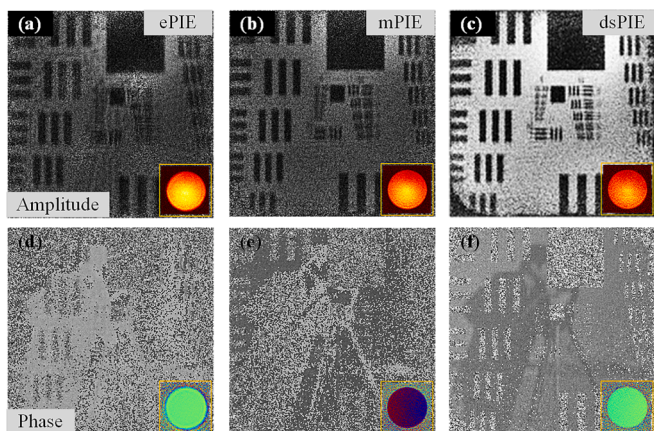


Fig. 6. Comparison of reconstructions for ePIE, mPIE, and dsPIE under a heavy mixture noise with a SNR of 15 dB. (a)–(c) The reconstructions of the rPIE, mPIE, and the proposed dsPIE, respectively. The corresponding reconstructed probes are displayed in the yellow insert within the subfigures. (For interpretation of the references to colour in this figure legend, the reader is referred to the web version of this article.)

reconstructed complex-valued object and the ground truth under Poisson noise with a SNR of 15 dB for ePIE, mPIE, and dsPIE, respectively, as presented in Fig. 8. It is observed that mPIE initially demonstrates a fast convergence speed within the first 50 iterations, but then starts to exhibit intense oscillations as the iterations progress. Whereas, ePIE shows a smoother variation throughout the entire process, but with lower levels of reconstruction quality. In contrast, dsPIE achieves a balanced convergence between speed and stability. It maintains a relatively fast convergence speed while also providing improved stability. The object remolding moments are clearly demonstrated, indicating that the convergence is enforced to jump out of local minima and reach a finer reconstruction globally. This is achieved by applying a specialized decision function to sparsely execute the remolding matrix in dsPIE. As a result, dsPIE generally achieves better convergence robustness against noise, even under heavy mixture noise conditions. The full evolution of the dsPIE reconstruction process is visually presented in a video sequence (Visualization 1) to illustrate how dsPIE dynamically jumps out of local minima and progressively converges to the optimal global solution during the iterative process at a heavy mixture noise with a SNR of 15 dB.

4. Experiments

In this section, we conducted proof-of-concept experiments in our laboratory to validate the proposed dsPIE method. The experimental setup is shown in Fig. 9. We utilized a narrowband filter at a center wavelength of 532 nm with a full width at half maximum (FWHM) of 3 nm (FL532-3, Thorlabs) to select a quasi-monochromatic radiation from the supercontinuum light source (SC-Pro, YSL Photonics). The beam was expanded through a beam expander (MODEL: GBE05-A, Thorlabs) with a magnification of 5, then focused onto the sample (R1L1S1N, Thorlabs) by a convex lens ($f = 50$ mm, MODEL: AC254-050-B-ML, Thorlabs) which generated a beam spot of about 200 μm in diameter. Diffraction occurred to the CMOS detector (QHY268M) in the far field at a distance of 50 mm. The sample was scanned laterally using an x-y linear stage (M-L01.1S0, PI) in a sequence of 11x11 overlapping adjacent grids, with an 80 μm step size. To mitigate periodic scanning ambiguity, a random lateral offset was introduced to the scanning intervals. As a result, a set of diffraction patterns was recorded by the detector as the sample moved through the illuminating beam. Additionally, the recorded diffraction patterns were merged to 256x256 pixels using 16x16-pixel binning to accelerate the reconstruction speed.

To obtain the diffraction dataset with varying levels of noise in ptychography, we first captured 10 frames of dark noise without beam illumination and calculated their average to measure the main profile of the dark current noise of the CMOS detector at 2 ms exposure time. Next, we generated a denoised diffraction dataset by performing a background noise removal approach to suppress the dark noise from the raw diffraction data [22]. Fig. 10(a) shows the denoised diffraction image with a SNR of 40 dB, while Fig. 10(e) shows the corresponding noisy diffraction image with a SNR of 26 dB for comparison. We then carried out the ptychographic reconstructions for the denoised diffraction dataset with a SNR of 40 dB. The reconstructed results after 500 iterations of ePIE, mPIE, and dsPIE are demonstrated in Fig. 10 (b)–(d), respectively. Noting that all these algorithms were performed under a common architecture, with the update function being the only variation. To ensure robustness against single random initialization in ptychography, we conducted 5 trails of each algorithm in every experiment, from which the best reconstruction was selected. As the results shown in Fig. 10 (b)–(d), all the algorithms demonstrated excellent reconstruction performance at high SNR levels. The line pairs in Group (7) / Element 3 of the retrieved USAF resolution target were clearly separated with high fidelity, as expected from the numerical simulation results. Among them, dsPIE achieved the best contrast and clarity, even in the edges of the reconstructed image where the overlapping information of illumination is less. In terms of resolution, ePIE showed the worst

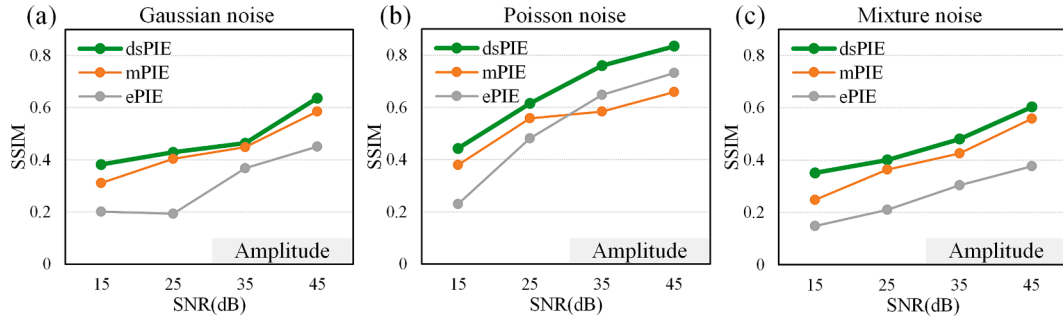


Fig. 7. The SSIM between the reconstructions and the ground truth across varying levels of noises. (a)–(c) show the SSIMs of the reconstructed object in amplitude across Gaussian noise, Poisson noise, and Mixture of Gaussian and Poisson noise, respectively.

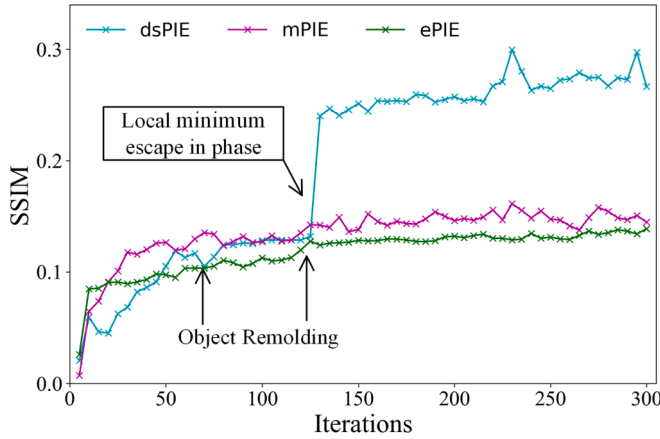


Fig. 8. Evolution of SSIM between the reconstructed complex-valued object and the ground truth for ePIE, mPIE, and dsPIE, respectively.

performance, while both mPIE and dsPIE achieved enhanced resolution.

To assess the robustness of the algorithms under higher noise levels, we increased the noise in the diffraction dataset to a SNR level of 26 dB, as shown in Fig. 10(e). The experimental reconstructions using ePIE, mPIE, and dsPIE were demonstrated in Fig. 10(f)–(h), respectively. When subjected to the heavily noised diffraction dataset, the reconstructed qualities of ePIE and mPIE deteriorate significantly, and the Group (6) of the retrieved USAF target cannot be distinguished with contrast. In contrast, dsPIE still presents a robust reconstruction against noise,

resulting in an improved resolution for the separation of the second element in Group (6) of the USAF target, as shown in the zoomed-in views in Fig. 10(h). Furthermore, the reconstructed probe of dsPIE reveals the features of the focused beam under noisy conditions, as shown in Fig. 10(i) for the amplitude and Fig. 10(j) for the phase. In Fig. 10(k), we utilized the Fourier ring correlation (FRC) [46] to quantify the resolution of the reconstructions for ePIE, mPIE, and dsPIE. The FRC is calculated between the reconstructions and the USAF target in design. It is evident that dsPIE achieves the best reconstructed resolution with voxel size of 8 nm given by the intersection of the FRC curve and an acceptable 0.143 threshold curve [47], outperforming ePIE and mPIE. This result is consistent with the retrieved USAF resolution target as demonstrated in Fig. 10(h).

Through further comparison of the PIE reconstruction results under different noise energies, it is evident that detector noise significantly hinders the convergence and results in a significant degradation of the reconstructed resolution and fidelity in ptychography. Although the proposed dsPIE algorithm effectively mitigates the impact of heavy mixture noises in ptychography, there is still an obvious decline in resolution (compared Fig. 10(h) with Fig. 10(d)). This resolution degradation, caused by the noise perturbation in diffraction signal measurement, becomes particularly pronounced in the presence of heavy noise. Therefore, improving the SNR of the diffraction signals in ptychography, especially for weak signals of higher diffraction orders, will be a key focus of our future research.

5. Discussion and conclusion

In summary, we proposed a novel approach called dsPIE that

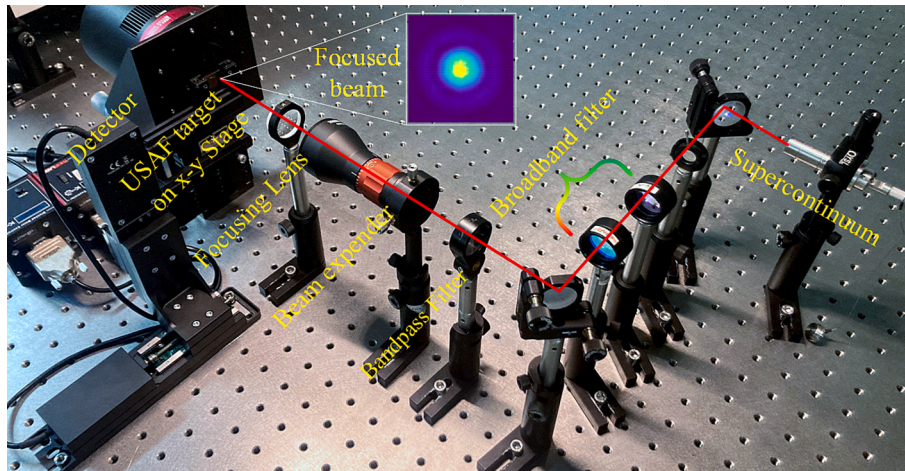


Fig. 9. Experimental setup. A quasi-monochromatic beam generated from supercontinuum light passing through a bandpass filter is expanded with a beam expander and focused onto the sample mounted on a x-y linear stage. A CMOS detector records a sequence of diffraction patterns as the sample is scanned laterally through the illuminated beam.

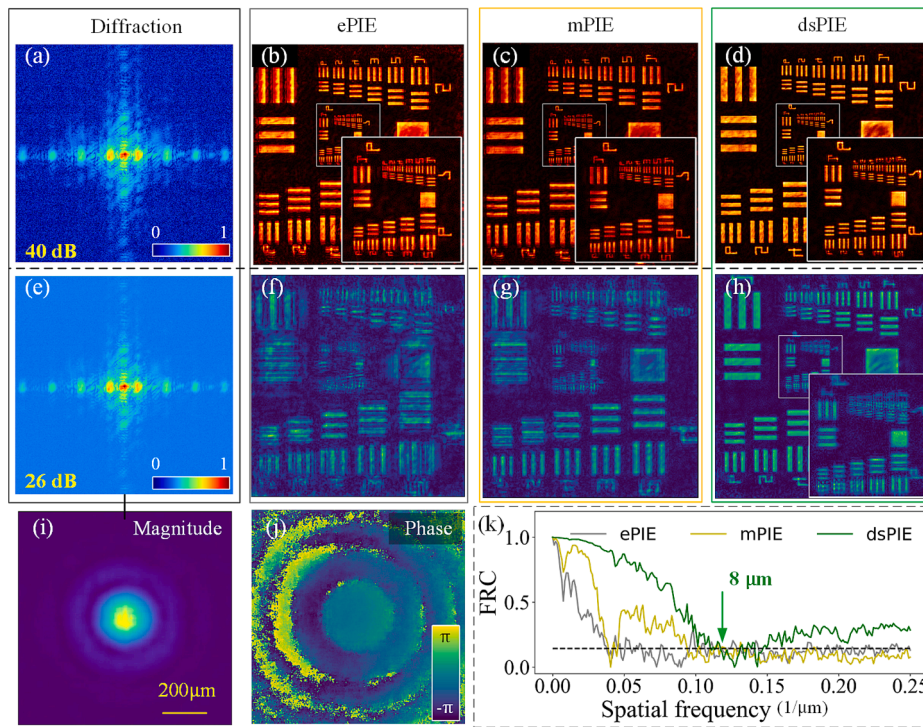


Fig. 10. Experimental results. (a) indicates a frame of the denoised diffraction data (40 dB SNR) by removing the CCD dark noise. (b)–(d) indicates the reconstructions from the denoised diffraction dataset of the ePIE, mPIE and dsPIE, respectively. (e) shows the raw noisy diffraction data (22 dB SNR). (f)–(h) indicates the reconstructions from the raw noisy diffraction dataset of the ePIE, mPIE and dsPIE, respectively. (i) and (j) give the magnitude and phase of the retrieved probe by dsPIE under a noisy condition, respectively. (g) FRC curves comparison along with a 0.143 threshold for ePIE, mPIE, and dsPIE, respectively. The diffraction images in (a) and (e) are scaled to $1/6$ power.

retrieves the global solution of a specimen and illuminated probe simultaneously to address problematic noisy datasets. Our proposed method involves optimizing the ptychographic exit wave update function using a dynamic sigmoid-remolding strategy. We present the basic working principle and operating process of dsPIE and demonstrate its advantages through three groups of proof-of-concept simulations and experiments. Our results show that dsPIE offers significantly improved robustness and stability in ptychographic reconstruction under heavy mixture detector noises compared to existing PIE algorithms. Specifically, dsPIE avoids converging to local minima and achieves preferable reconstruction quality, especially in cases of high-noised diffraction datasets.

The dsPIE is an improved phase retrieval method designed for practical applications. It uses adaptive regularized optimization with a dynamic sigmoid decision function to handle challenging mixed datasets and improve the robustness against noise.

Data availability

Data underlying the results presented in this paper are not publicly available at this time but may be obtained from the authors upon reasonable request.

Funding

This work was supported by the National Natural Science Foundation of China (52130504), Key Research and Development Program of Hubei Province (2021BAA013), Innovation Project of Optics Valley Laboratory (OVL2023PY003), Fundamental Research Funds for the Central Universities (2021XXJS113), and Guangdong Basic and Applied Basic Research Foundation (2023A1515030149).

Declaration of Competing Interest

The authors declare that they have no known competing financial

interests or personal relationships that could have appeared to influence the work reported in this paper.

Data availability

Data will be made available on request.

Acknowledgments

The authors thank the technical support from the Experiment Centre for Advanced Manufacturing and Technology in School of Mechanical Science & Engineering of HUST.

Appendix A. Supplementary data

Supplementary data to this article can be found online at <https://doi.org/10.1016/j.optlastec.2023.110510>.

References

- [1] R.W. Gerchberg, W.O. Saxton, A Practical Algorithm for the Determination of Phase from Image and Diffraction Plane Pictures, *Optik (stuttgart)* 35 (1972) 237–246.
- [2] J.M. Rodenburg, H.M.L. Faulkner, A phase retrieval algorithm for shifting illumination, *Appl Phys Lett* 85 (2004) 4795–4797, <https://doi.org/10.1063/1.1823034>.
- [3] A.M. Maiden, M.J. Humphry, F. Zhang, J.M. Rodenburg, Superresolution imaging via ptychography, *J Opt Soc Am A* 28 (2011) 604–612, <https://doi.org/10.1364/josaa.28.000604>.
- [4] D.F. Gardner, M. Tanksalvala, E.R. Shanblatt, X. Zhang, B.R. Galloway, C.L. Porter, et al., Subwavelength coherent imaging of periodic samples using a 13.5 nm tabletop high-harmonic light source, *Nat Photonics* 11 (2017) 259–263, <https://doi.org/10.1038/nphoton.2017.33>.
- [5] P. Li, M. Allain, T.A. Grünwald, M. Rommel, A. Campos, D. Carbone, et al., 4Th Generation Synchrotron Source Boosts Crystalline Imaging At the Nanoscale, *Light Sci Appl* 11 (2022) 1–12, <https://doi.org/10.1038/s41377-022-00758-z>.

- [6] R.N. Wilke, M. Priebe, M. Bartels, K. Giewekemeyer, A. Diaz, P. Karvinen, et al., Hard X-ray imaging of bacterial cells: nano-diffraction and ptychographic reconstruction, *Opt Express* 20 (2012) 19232–19254, <https://doi.org/10.1364/oe.20.019232>.
- [7] A. Pan, C. Zuo, B. Yao, High-resolution and large field-of-view Fourier ptychographic microscopy and its applications in biomedicine, *Reports Prog Phys* 83 (2020), 096101, <https://doi.org/10.1088/1361-6633/aba6f0>.
- [8] M. Wan, J.J. Healy, J.T. Sheridan, Terahertz phase imaging and biomedical applications, *Opt Laser Technol* 122 (2020), 105859, <https://doi.org/10.1016/j.optlastec.2019.105859>.
- [9] B. Zhang, D.F. Gardner, M.D. Seaberg, E.R. Shanblatt, H.C. Kapteyn, M. Murnane, et al., High contrast 3D imaging of surfaces near the wavelength limit using tabletop EUV ptychography, *Ultramicroscopy* 158 (2015) 98–104, <https://doi.org/10.1016/j.ultramicro.2015.07.006>.
- [10] M. Holler, M. Guizar-Sicairos, E.H.R. Tsai, R. Dinapoli, E. Müller, O. Bunk, et al., High-resolution non-destructive three-dimensional imaging of integrated circuits, *Nature* 543 (2017) 402–406, <https://doi.org/10.1038/nature21698>.
- [11] P. Thibault, A. Menzel, Reconstructing state mixtures from diffraction measurements, *Nature* 494 (2013) 68–71, <https://doi.org/10.1038/nature11806>.
- [12] J. Huijts, S. Fernandez, D. Gauthier, M. Kholodstova, A. Maghraoui, K. Medjoubi, et al., Broadband coherent diffractive imaging, *Nat Photonics* 14 (2020) 618–622, <https://doi.org/10.1038/s41566-020-0660-7>.
- [13] P. Dwivedi, A.P. Konijnenberg, S.F. Pereira, H.P. Urbach, Lateral position correction in ptychography using the gradient of intensity patterns, *Ultramicroscopy* 192 (2018) 29–36, <https://doi.org/10.1016/j.ultramicro.2018.04.004>.
- [14] M. Beckers, T. Senkbeil, T. Gorniak, K. Giewekemeyer, T. Salditt, A. Rosenhahn, Drift correction in ptychographic diffractive imaging, *Ultramicroscopy* 126 (2013) 44–47, <https://doi.org/10.1016/j.ultramicro.2012.11.006>.
- [15] L. Rong, C. Tang, D. Wang, B. Li, F. Tan, Y. Wang, et al., Probe position correction based on overlapped object wavefront cross-correlation for continuous-wave terahertz ptychography, *Opt Express* 27 (2019) 938, <https://doi.org/10.1364/OE.27.000938>.
- [16] T. Ruan, W. Lv, Y. Tao, J. Zhang, X. Yan, D. Yang, et al., Adaptive total variation based autofocusing strategy in ptychography, *Opt Lasers Eng* 158 (2022), 107136, <https://doi.org/10.1016/j.optlaseng.2022.107136>.
- [17] L. Loetgering, M. Du, K.S.E. Eikema, S. Witte, zPIE: an autofocusing algorithm for ptychography, *Opt Lett* 45 (2020) 2030, <https://doi.org/10.1364/ol.389492>.
- [18] W. Tang, J. Yang, W. Yi, Q. Nie, J. Zhu, M. Zhu, et al., Single-shot coherent power-spectrum imaging of objects hidden by opaque scattering media, *Appl Opt* 58 (2019) 1033, <https://doi.org/10.1364/AO.58.001033>.
- [19] X. Wen, Y. Geng, X. Zhou, J. Tan, S. Liu, C. Tan, et al., Ptychography imaging by 1-D scanning with a diffuser, *Opt Express* 28 (2020) 22658, <https://doi.org/10.1364/OE.399184>.
- [20] W. Tang, Y. Guo, W. Yi, J. Yang, J. Zhu, W. Wang, et al., A robust fast variable-aperture Fourier ptychography, *Opt Commun* 443 (2019) 144–149, <https://doi.org/10.1016/j.optcom.2019.03.004>.
- [21] L. Li, A. Pan, C. Li, H. Zhao, Co-phase error detection for segmented mirrors with ptychography, *Opt Commun* 537 (2023), 129393, <https://doi.org/10.1016/j.optcom.2023.129393>.
- [22] C. Wang, Z. Xu, H. Liu, Y. Wang, J. Wang, R. Tai, Background noise removal in x-ray ptychography, *Appl Opt* 56 (2017) 2099, <https://doi.org/10.1364/AO.56.002099>.
- [23] M. Odstrčil, A. Menzel, M. Guizar-Sicairos, Iterative least-squares solver for generalized maximum-likelihood ptychography, *Opt Express* 26 (2018) 3108, <https://doi.org/10.1364/oe.26.003108>.
- [24] Z. Qiao, X. Wen, X. Zhou, F. Qin, S. Liu, B. Gao, et al., Adaptive iterative guided filtering for suppressing background noise in ptychographical imaging, *Opt Lasers Eng* 160 (2023), 107233, <https://doi.org/10.1016/j.optlaseng.2022.107233>.
- [25] A. Maiden, D. Johnson, P. Li, Further improvements to the ptychographical iterative engine, *Optica* 4 (2017) 736, <https://doi.org/10.1364/OPTICA.4.000736>.
- [26] X. Wu, J. Zhao, G. Cui, H. Mao, A lensless LED matrix-based ptychographic microscopy imaging method using loss correction and adaptive step size, *Opt Lasers Eng* 152 (2022), 106980, <https://doi.org/10.1016/j.optlaseng.2022.106980>.
- [27] C. Zuo, J. Sun, Q. Chen, Adaptive step-size strategy for noise-robust Fourier ptychographic microscopy, *Opt Express* 24 (2016) 20724, <https://doi.org/10.1364/OE.24.020724>.
- [28] A.M. Maiden, J.M. Rodenburg, An improved ptychographical phase retrieval algorithm for diffractive imaging, *Ultramicroscopy* 109 (2009) 1256–1262, <https://doi.org/10.1016/j.ultramicro.2009.05.012>.
- [29] S. Marchesini, H. He, N. Chapman, P. Hau-Riege, A. Noy, R. Howells, et al., X-ray image reconstruction from a diffraction pattern alone, *Phys Rev B - Condens Matter Mater Phys* 68 (2003) 1–5, <https://doi.org/10.1103/PhysRevB.68.140101>.
- [30] P. Godard, G. Carbone, M. Allain, F. Mastropietro, G. Chen, L. Capello, et al., Three-dimensional high-resolution quantitative microscopy of extended crystals, *Nat Commun* 2 (2011) 1–6, <https://doi.org/10.1038/ncomms1569>.
- [31] G. Zheng, R. Horstmeyer, C. Yang, Wide-field, high-resolution Fourier ptychographic microscopy, *Nat Photonics* 7 (2013) 739–745, <https://doi.org/10.1038/nphoton.2013.187>.
- [32] G.E. Healey, R. Kondepudy, Radiometric CCD Camera Calibration and Noise Estimation, *IEEE Trans PATTERN Anal Mach Intell* 16 (1994).
- [33] S.W. Hasinoff, F. Durand, W.T. Freeman, Noise-optimal capture for high dynamic range photography, *IEEE Comput. Soc. Conf. Comput. Vis. Pattern Recognit IEEE* 2010 (2010) 553–560, <https://doi.org/10.1109/CVPR.2010.5540167>.
- [34] Rodenburg J, Maiden A. Ptychography. In: P.W. Hawkes, J.C.H. Spence, editors. *Springer Handb. Microsc.*, Springer International Publishing.; 2019, p. 819–904. 10.1007/978-3-030-00069-1_17.
- [35] Yang C, Qian J, Schirotzek A, Maia F, Marchesini S. Iterative Algorithms for Ptychographic Phase Retrieval. *ArXiv Prepr ArXiv* 2011:1105.5628.
- [36] L. Bian, J. Suo, G. Zheng, K. Guo, F. Chen, Q. Dai, Fourier ptychographic reconstruction using Wirtinger flow optimization, *Opt Express* 23 (2015) 4856, <https://doi.org/10.1364/oe.23.004856>.
- [37] S. Boyd, L. Vandenberghe, *Convex Optimization*, 7th ed., Cambridge University Press (CUP), 2009.
- [38] P. Thibault, M. Dierolf, O. Bunk, A. Menzel, F. Pfeiffer, Probe retrieval in ptychographic coherent diffractive imaging, *Ultramicroscopy* 109 (2009) 338–343, <https://doi.org/10.1016/j.ultramicro.2008.12.011>.
- [39] D.R. Luke, Relaxed averaged alternating reflections for diffraction imaging, *Inverse Probl* 21 (2005) 37–50, <https://doi.org/10.1088/0266-5611/21/1/004>.
- [40] P. Ansuinelli, W.M.J. Coene, H.P. Urbach, Refinement strategies for optimal inclusion of prior information in ptychography, *Proc SPIE* 11517 (2020) 1151711, <https://doi.org/10.1117/12.2572019>.
- [41] Z. Wang, A.C. Bovik, H.R. Sheikh, E.P. Simoncelli, Image Quality Assessment: From Error Visibility to Structural Similarity, *IEEE Trans Image Process* 13 (2004) 600–612, <https://doi.org/10.1109/TIP.2003.819861>.
- [42] A.M. Maiden, M.J. Humphry, M.C. Sarahan, B. Kraus, J.M. Rodenburg, An annealing algorithm to correct positioning errors in ptychography, *Ultramicroscopy* 120 (2012) 64–72, <https://doi.org/10.1016/j.ultramicro.2012.06.001>.
- [43] H. Chang, Y. Lou, Y. Duan, S. Marchesini, Total Variation-Based Phase Retrieval for Poisson Noise Removal, *SIAM J Imaging Sci* 11 (2018) 24–55, <https://doi.org/10.1137/16M1103270>.
- [44] Y. Zhang, P. Song, Q. Dai, Fourier ptychographic microscopy using a generalized Anscombe transform approximation of the mixed Poisson-Gaussian likelihood, *Opt Express* 25 (2017) 168, <https://doi.org/10.1364/OE.25.000168>.
- [45] D. Penagos Molina, L. Loetgering, W. Eschen, J. Limpert, J. Rothhardt, Broadband ptychography using curved wavefront illumination, *Opt Express* (2023), <https://doi.org/10.1364/OE.495197>.
- [46] W.O. Saxton, W. Baumeister, The correlation averaging of a regularly arranged bacterial cell envelope protein, *J Microsc* 127 (1982) 127–138, <https://doi.org/10.1111/j.1365-2818.1982.tb00405.x>.
- [47] M. van Heel, M. Schatz, Fourier shell correlation threshold criteria, *J Struct Biol* 151 (2005) 250–262, <https://doi.org/10.1016/j.jsb.2005.05.009>.